Supplementary Material for

Remote HVGD Implying the Seismogenic Positions of 2025 Mandalay Earthquake Sequence

Yu Feng[1,2], Wenfei Mao[1,2*], Jia Li[1,2], Yifan Ding[1,2], Yuan Qi[3], Guokun Chen[4,5], Busheng Xie[6], Licheng Sun[1,2], Hong Tang[7], Lixin Wu[1,2*]

[1] School of Geoscience and Info-Physics, Central South University, Changsha, 410083, China.
[2] Laboratory of Geo-Hazards Perception, Cognition and Predication, Central South University, Changsha, 410083, China.
[3] Department of Geography, Faculty of Social Sciences, The University of Hong Kong, Hong Kong SAR, China.
[4] Faculty of Land and Resources Engineering, Kunming University of Science and Technology, Kunming 650093, China.
[5] Yunnan Key Laboratory of Quantitative Remote Sensing, Kunming University of Science and Technology, Kunming 650093, China.
[6] Guangdong Provincial Disaster Prevention and Mitigation Center, Guangzhou 510630, China.
[7] Faculty of Geographical Science, Beijing Normal University, Beijing 100875, China.
Corresponding author: Wenfei Mao (maowf2014@126.com); Lixin Wu (wulx66@csu.edu.cn)

Table of Contents

Text S1.

Detailed information of the YNCH station.

The data acquisition system of the YNCH station is a wireless framework consisting of three modules: a sensor module, a power supply module, and a data transmission & management module. The sensor module is an F901-T triaxial fluxgate digital sensor manufactured by Coly GmbH, Germany. The power supply module primarily operates through charging via solar panel, energy storage in battery, and controlled power discharge via the output terminal of the controller. The data transmission & management module mainly consists of the DTU (Data Transfer Unit) and a cloud platform for data reception. the detailed photos of the YNCH station are shown as Fig. S1.

The raw geomagnetic data collected at the YNCH station are shown in Fig. S2. The geomagnetic field was strongly influenced by solar activity and geomagnetic storms, as illustrated in Fig. S3 and S4, which present the amplitude variations of the three components caused by these factors. These influences were consistent with the global characteristics of geomagnetic storm impacts.

Text S2.

Preprocess of geomagnetic data.

The abnormally high value is the geomagnetic component value whose absolute deviation from the overall median exceeds 3000 nT. A spline interpolation method was employed to interpolate the daily geomagnetic data to a total of 86,400. A moving average method was applied to smooth the 1-second geomagnetic data to a 1-minute resolution. For a sliding window of size *k*, the average was computed over $(k-1)/2$ elements preceding and following the current element, with the current element as the center. In the case of an even *k*, the central element was included in the segment comprising the first $(k-1)/2$ elements. The case of moving average method is shown in Fig. S5.

Text S3.

Intersection between the normal equation and the fault line equation.

Assuming the geomagnetic station coordinate is (x_1, y_1), the remote endpoint (x_2, y_2) can be determined from the X-component and Y-component geomagnetic disturbance variations (dB_x, dB_y). Consequently, the normal equation of geomagnetic disturbance vector can be established by using these two points.

$$\begin{cases} Ax + By + C = 0 \\ A = y_2 - y_1 \\ B = x_2 - x_1 \\ C = x_2 y_1 - x_1 y_2 \end{cases} \tag{1}$$

The fault line is composed of multiple segments. Thus, for a segment defined by its starting point (x_{f1}, y_{f1}) and ending point (x_{f2}, y_{f2}), its linear equation can be determined:

$$\begin{cases} A_1x + B_2y + C_3 = 0 \\ A_1 = y_{f2} - y_{f1} \\ B_1 = x_{f2} - x_{f1} \\ C_1 = x_{f2}y_{f1} - x_{f1}y_{f2} \end{cases} \quad (2)$$

To find the intersection point, it is first necessary to determine whether they intersect. This is assessed by defining a discriminant as follows:

$$g = AB_1 + BA_1 \quad (3)$$

The lines are parallel when g=0, and the calculation halts; when $g \neq 0$, the intersection point is solved as follows:

Step 1: Establish a parametric equation for the fault segment, where any point P on it can be expressed by a parameter t as:

$$\begin{cases} x(t) = x_{f1} + t(x_{f2} - x_{f1}) \\ y(t) = y_{f1} + t(y_{f2} - y_{f1}) \end{cases} \quad (4)$$

Where: t=0 and t=1 correspond to the start and end points, respectively, and any value which is satisfied $0 < t < 1$ defines an interior point on the segment.

The intersection point satisfies the normal equation. Substitution and simplification lead to:

$$Ax_{f1} + By_{f1} + C + t[A(x_{f2} - x_{f1}) + B(y_{f2} - y_{f1})] = 0 \quad (5)$$

The solution for the parameter t is given by the following equation:

$$t = \frac{-(Ax_{f1} + By_{f1} + C)}{g} \quad (6)$$

The next step is performed only if the condition $0 \leqslant t \leqslant 1$, calculated via Eq. (6), is met, confirming that the intersection points lie on the segment.

Step 2: Check whether the intersection point is located on the ray line which is defined by right-hand rule. This is equivalent to verifying whether the azimuth of the ray from the station to the intersection point satisfies the following condition relative to the azimuth of the magnetic disturbance vector:

$$\alpha = \alpha_1 - 90^\circ \quad (7)$$

Where α is the azimuth of the ray from the station to the intersection point, and α_1 is the azimuth of the magnetic disturbance vector.

Once both conditions, $0 \leqslant t \leqslant 1$ and Equation (7), are satisfied, the intersection point between the normal equation and this fault segment can be solved by using Eq. (4).

The detailed calculate process is shown as Fig. S6.

The temporal variation in the total count of intersection points in the study area during March 23-31 is shown as Fig. S7. The analysis of time periods with Kp ≤4 on March 24th, 26th, and 27th is shown as Fig. S8.

Text S4.

Approximate magnetic permeability of underground rockmass.

The conductor transmitting PSRC from the epicenter to the surface consists of rockmass, and it is surrounded by magnetized rockmass during transmission. Therefore, the magnetic permeability in the Biot-Savart law must be corrected according to the magnetic properties of these rockmass. Based on empirical assessment of iron content[1] and serpentinization in the Sagaing Fault[2], the magnetic susceptibility of rockmass near the fault zone is estimated to be approximately 40×10^{-3} SI. This corresponds to a relative magnetic permeability (u_r) of approximately 1.04. Therefore, the magnetic permeability (u) used in the Biot-Savart law for current inversion calculations should be updated to $\mu = u_r\mu_0 = 4.16\pi\times10^{-7}$ H/m.

Text S5.

Calculation of current density area about MBT anomaly results.

The MBT anomaly results for the period 2020–2025 and for the specific period March 23–31, 2025, are shown in Fig. S9 and S10, respectively.

When the residual MBT exceeds 12 ($\Delta MBT > 12$), it can be identified as an obvious MBT positive anomaly. The resolution of all MBT anomaly analysis results in this study is 0.05°N × 0.05°E. Therefore, the total area of the MBT positive anomaly was calculated by summing the pixel areas which satisfy $\Delta MBT > 12$. Considering the effect of latitude on east–west distances, each pixel with a resolution of 0.05° × 0.05° was calculated according to the Eq. (8).

$$A = 0.05^2 \left(\frac{\pi}{180}\right)^2 R^2 * La * Lo * \cos(La) \tag{8}$$

Where, A is the area of the MBT positive anomaly of each pixel with a resolution of 0.05° × 0.05°, R is the approximate Earth radius, taken as 6371 km, La is the latitude of the pixel, and Lo is the longitude of the pixel.

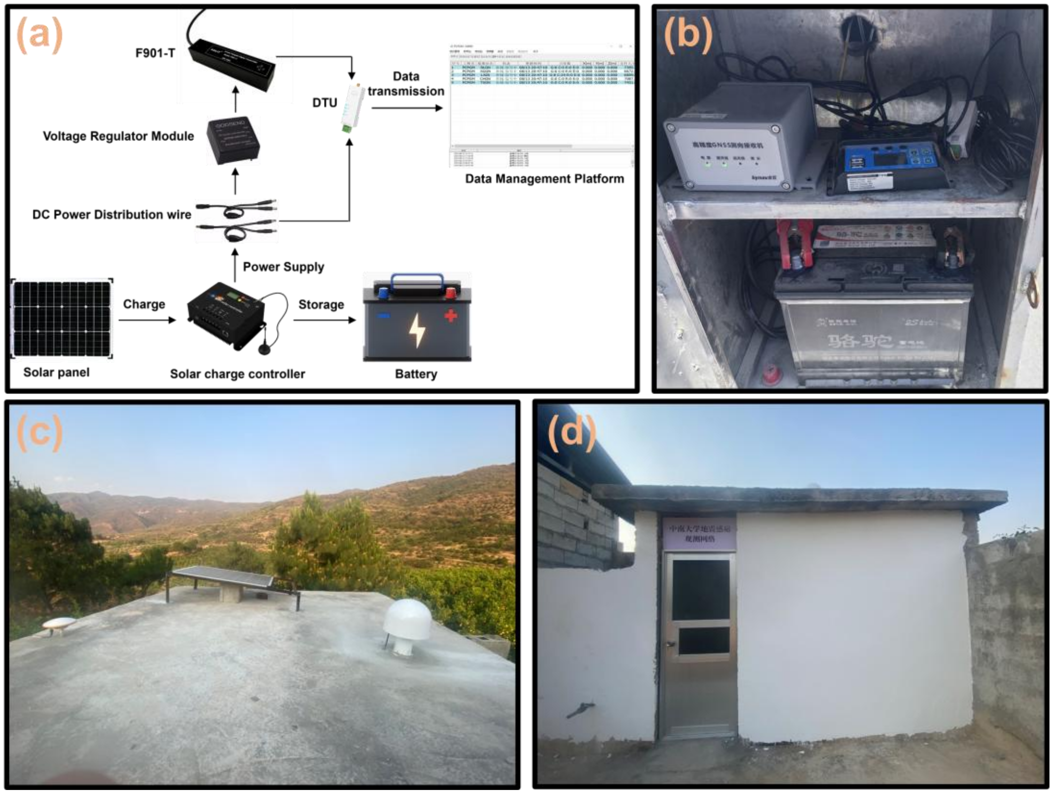

Figure S1. Detailed information of the YNCH station. (a) The frame of data acquisition system. The F901-T is used to obtain the geomagnetic data. The DTU is used to transmission data. The power supply module primarily operates through charging via solar panel, storage in battery, and controlled discharge from the output terminal of the solar charge controller. **(b) (c) and (d)** Photos of the YNCH station.

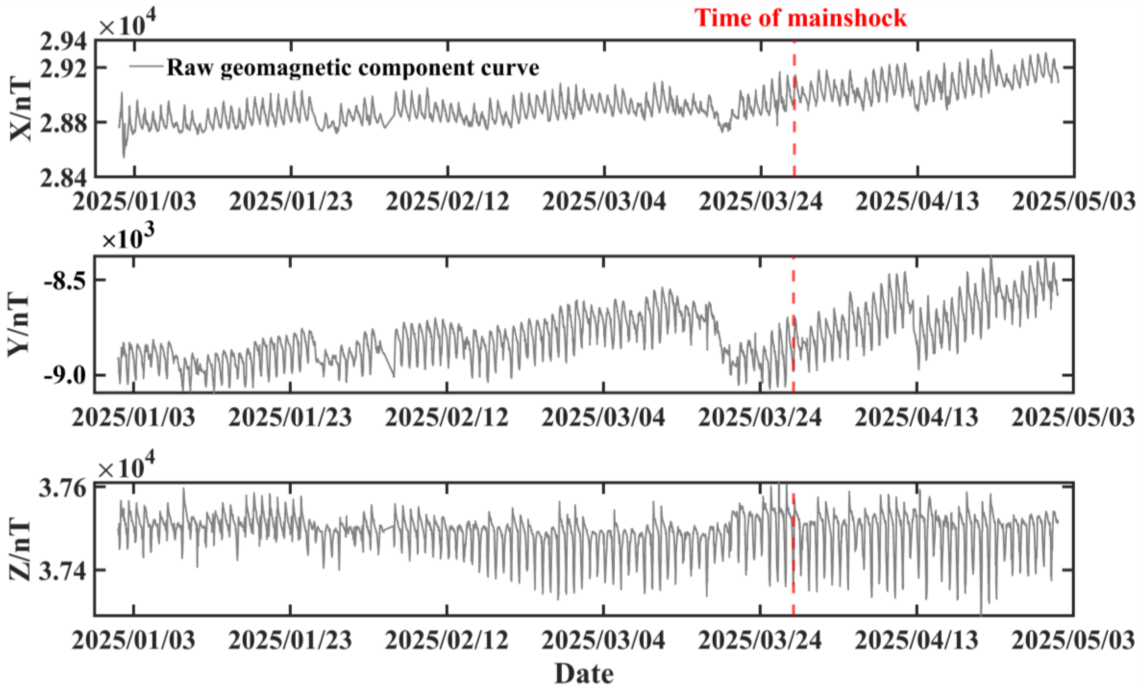

Figure S2. The long-term raw geomagnetic component data recorded at the YNCH station from January to April 2025.

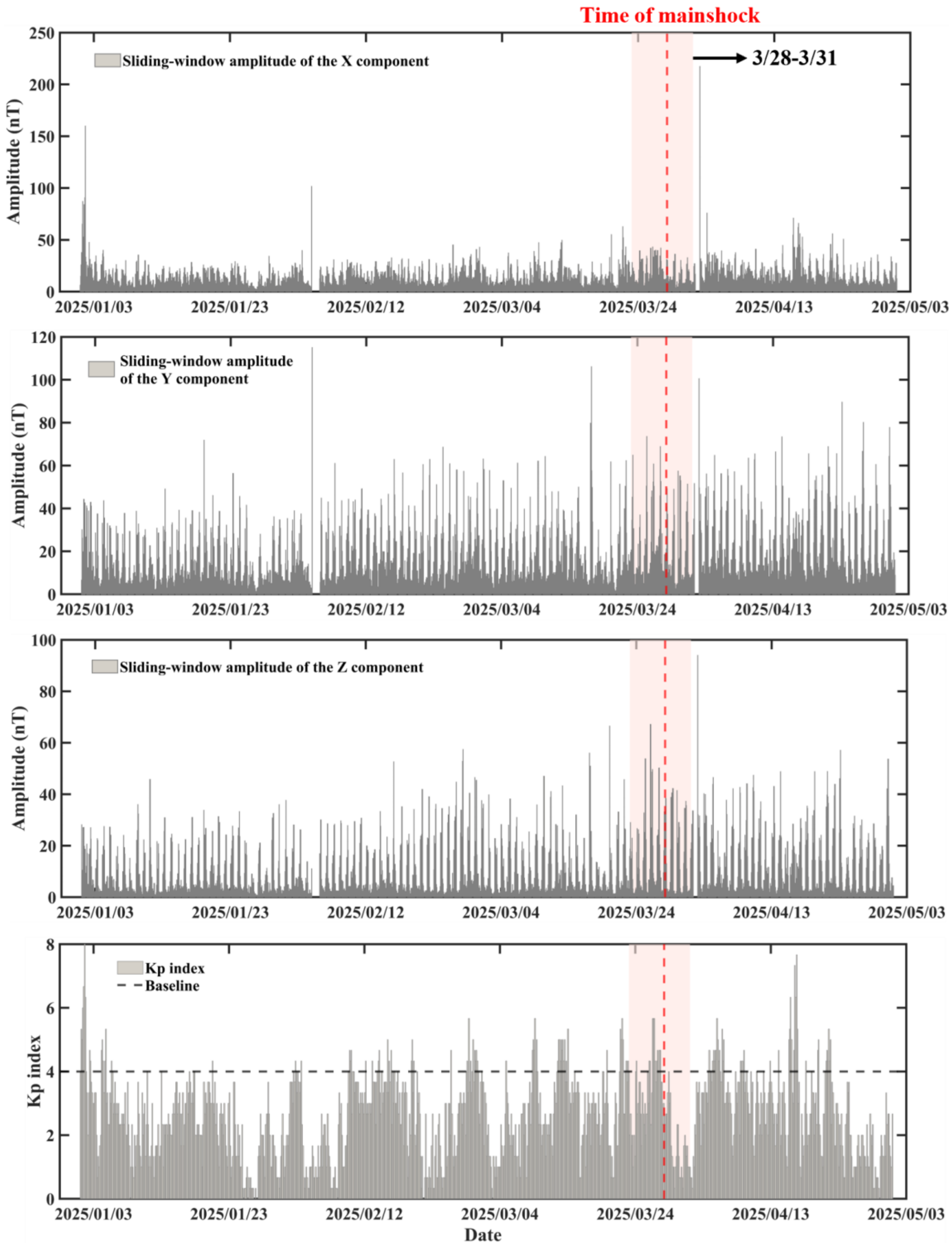

Figure S3. Geomagnetic amplitude variation curves affected by solar activity and geomagnetic storms (January–April 2025). Amplitudes were computed using a 10-minute sliding window. The figure reveals a strong correlation between amplitudes and geomagnetic storms, especially for the X and Y components.

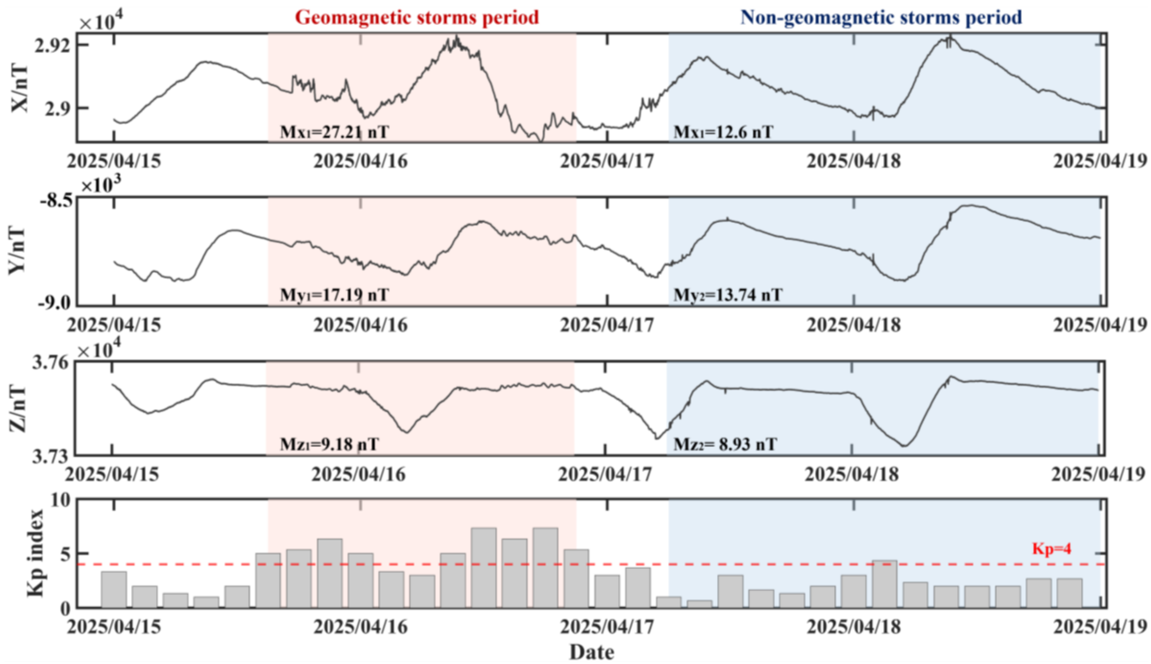

Figure S4. Typical variations in geomagnetic data amplitude during geomagnetic storms and non-geomagnetic storms periods. Mx_1, My_1, and Mz_1 represents the average amplitudes of the X, Y, and Z components respectively during the geomagnetic storm period, computed within the region using a 10-minute sliding window. Mx_2, My_2, and Mz_2 represents the average amplitudes of the X, Y, and Z components respectively during the non-geomagnetic storms period, computed within the region using a 10-minute sliding window. Compared with the Z component, the horizontal components are more significantly affected by geomagnetic storms. These influences were consistent with the global characteristics of geomagnetic storm impacts.

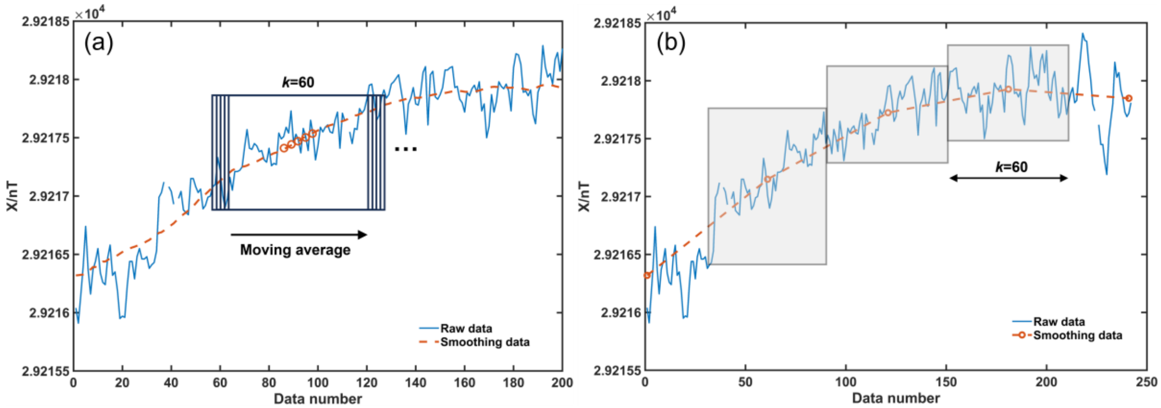

Figure S5. The case of moving average method. (a) The principle of the moving average calculation. The sliding window has a step size of 1 data and a window size of 60 data, representing a 1-minute interval. **(b)** Moving average smoothing of geomagnetic data resampled from 1-second to 1-minute resolution. The raw geomagnetic data are recorded at a 1-second sampling rate, and the smoothed 1-minute resolution data shown in (b) are utilized for the intersection calculation.

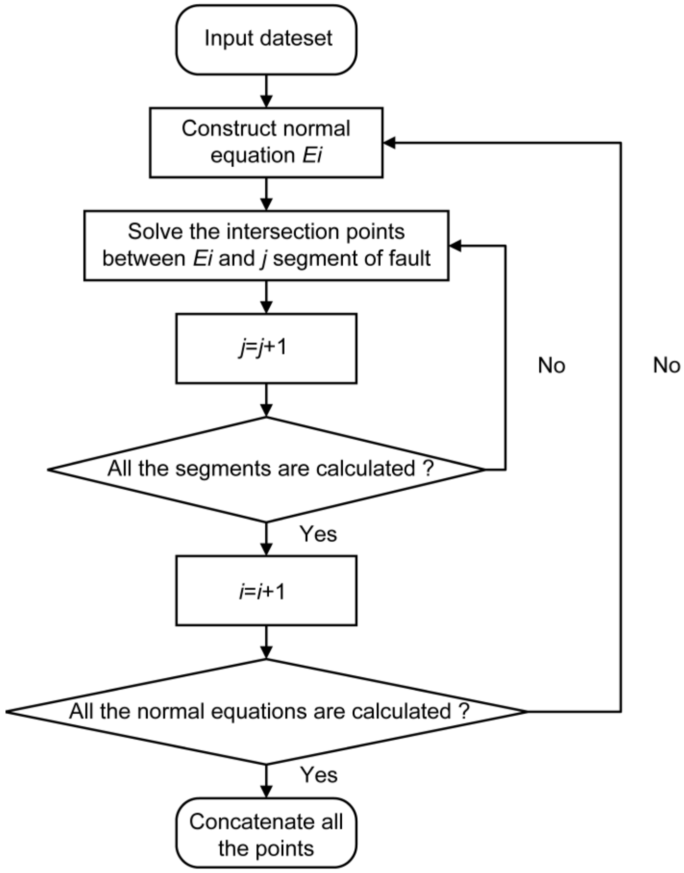

Figure S6. The flowchart of the intersection method. For each minute, the recognized HVGD can be used to formulate a normal ray equation. The fault line is represented by 241 parametric equations corresponding to its segments. The results of the forward intersection are obtained by solving for the intersection points between the per-minute normal ray equation and the parametric equations of all fault segments.

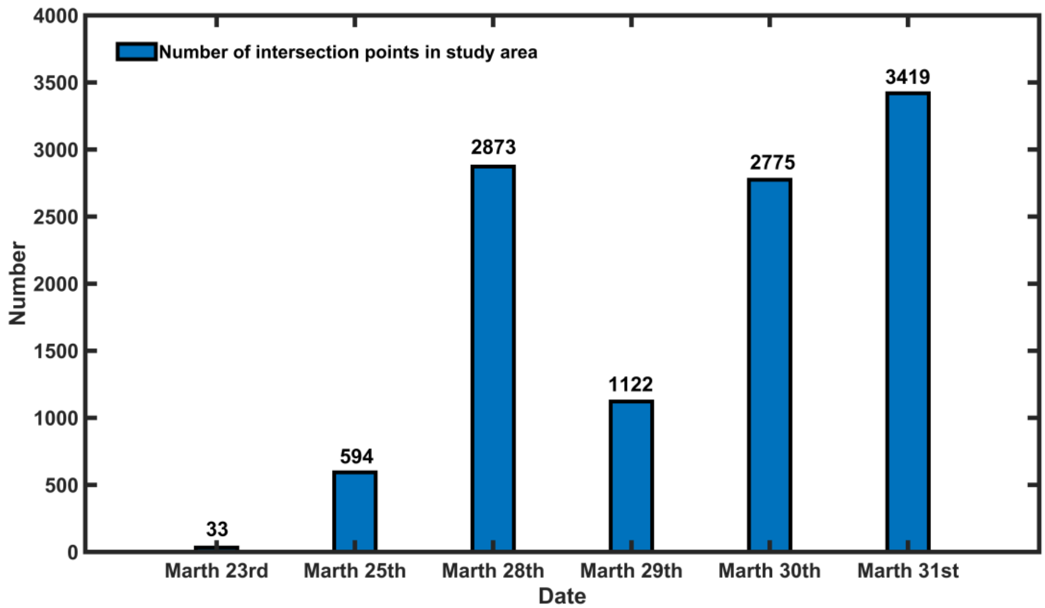

Figure S7. Temporal variation in the total count of intersection points in the study area.

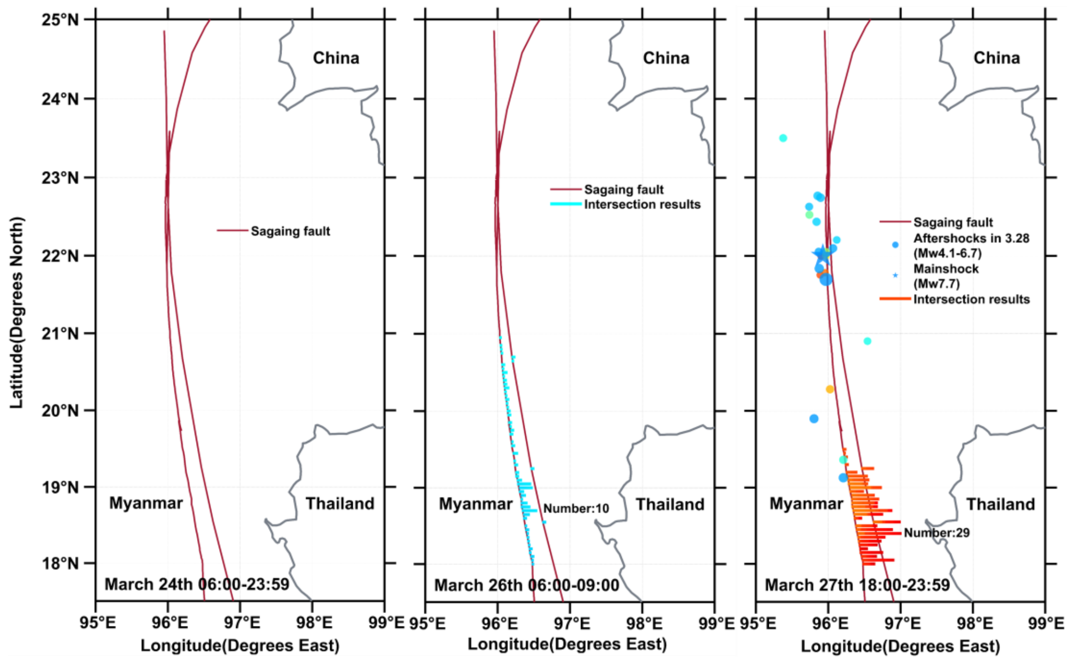

Figure S8. Supplementary analysis results for March 24, 26, and 27th. Time intervals characterized by a Kp ≤ 4 were observed from 06:00 to 23:59 UTC on March 24, from 06:00 to 09:00 UTC on March 26, and from 18:00 to 23:59 UTC on March 27.

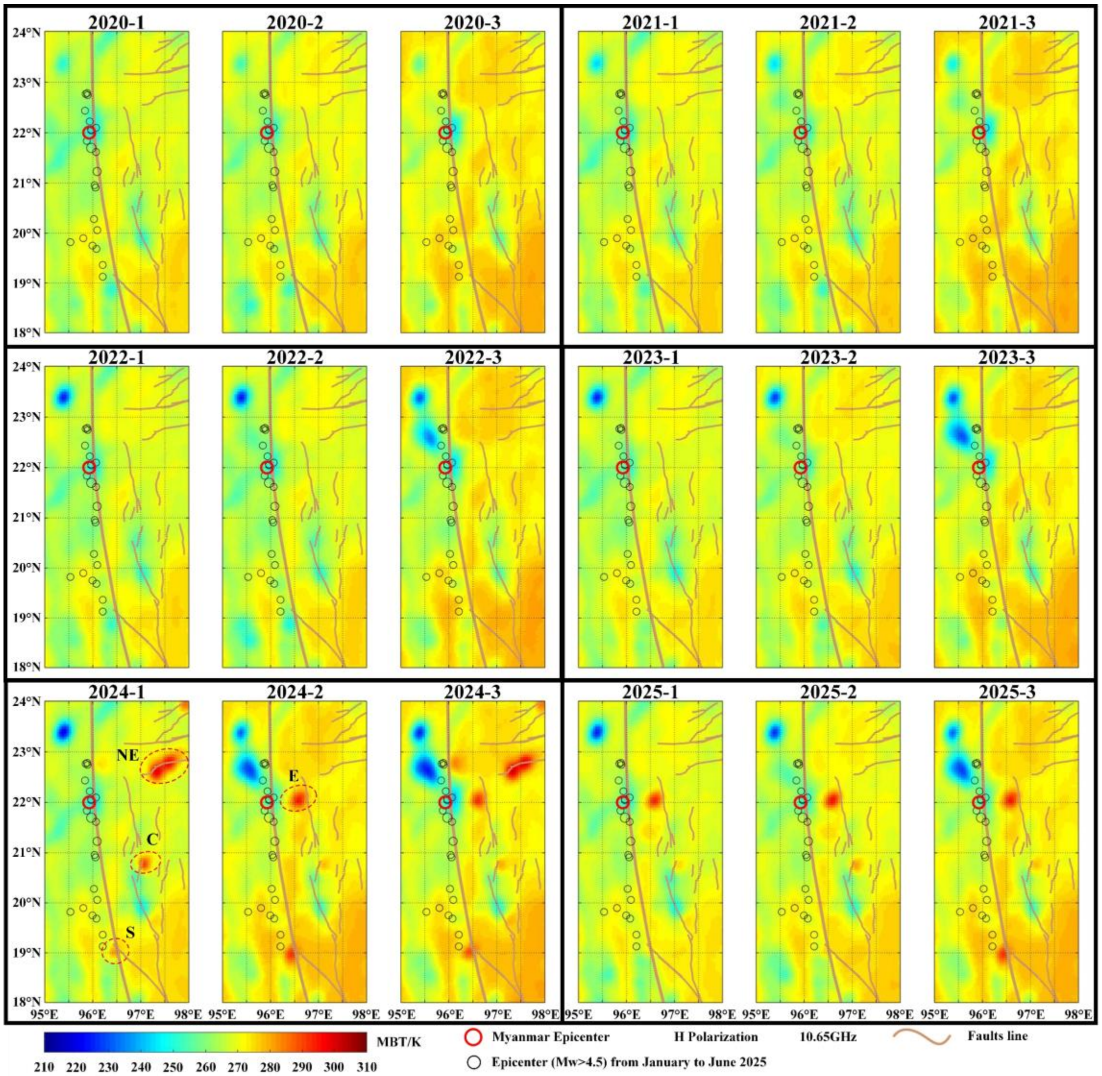

Figure S9. MBT anomaly analysis results about PSRC for the Mandalay Mw 7.7 earthquake during 2020-2025.

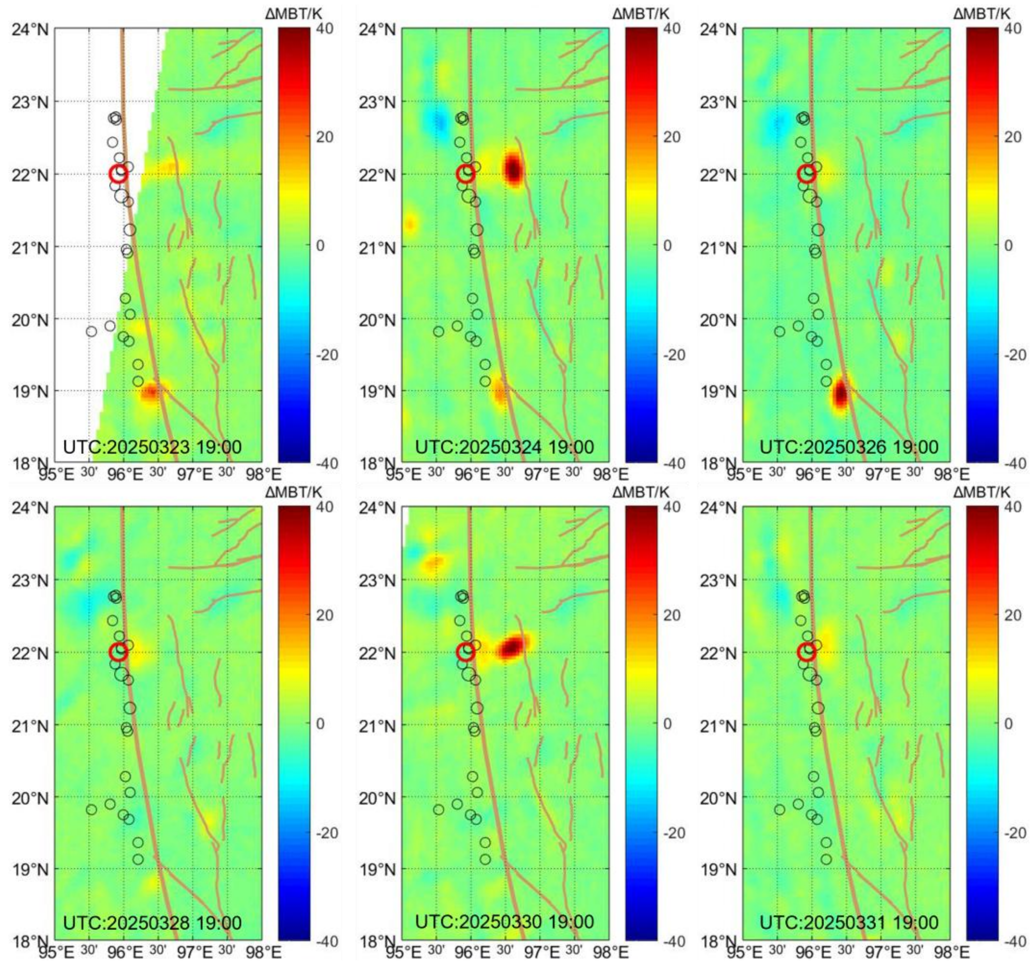

Figure S10. Results of MBT anomaly analysis from March 23rd to March 31st. Pre-seismic MBT positive anomalies were primarily located south of the fault, showing strong connection with the distribution of intersection points. Post-seismically, these anomalies were concentrated around areas with high densities of intersection points.

Supplementary Material References

1. Khant, N., Piestrzynski, A. & Lim, C. Geology, geochemistry, mineralogy of Phayaung Taung, Patheingyi Township, Mandalay Division, Myanmar. Geosci J. 25, 145–156 (2021).
2. Morishita, T. et al. Origin and Evolution of Ultramafic Rocks along the Sagaing Fault, Myanmar. J. Earth Sci. 34, 122–132 (2023).